



Title	Magnetic interactions in praseodymium ruthenate Pr_3RuO_7 with fluorite-related structure
Author(s)	Inabayashi, Masaki; Doi, Yoshihiro; Wakeshima, Makoto; Hinatsu, Yukio
Citation	Journal of Solid State Chemistry, 250, 100-106 https://doi.org/10.1016/j.jssc.2017.03.025
Issue Date	2017-06
Doc URL	http://hdl.handle.net/2115/74533
Rights	©2017. This manuscript version is made available under the CC-BY-NC-ND 4.0 license https://creativecommons.org/licenses/by-nc-nd/4.0/
Rights(URL)	https://creativecommons.org/licenses/by-nc-nd/4.0/
Type	article (author version)
File Information	manuscript_79280.pdf



[Instructions for use](#)

Magnetic Interactions in Praseodymium Ruthenate Pr_3RuO_7 with Fluorite-related Structure

Masaki Inabayashi, Yoshihiro Doi, Makoto Wakeshima and Yukio Hinatsu

Division of Chemistry, Graduate School of Science, Hokkaido University, Sapporo 060-0810,

Japan

Corresponding author, tel/fax:+81-11-706-2702

E-mail address: hinatsu@sci.hokudai.ac.jp

Key-words: Magnetic properties; Praseodymium; Ruthenium; Oxides; Antiferromagnetic transition

Abstract

Solid solutions $\text{Pr}_3(\text{Ru}_{1-x}\text{Ta}_x)\text{O}_7$ ($0 \leq x \leq 1.0$) and $(\text{Pr}_{1-x}\text{Y}_x)_3\text{RuO}_7$ ($0 \leq x \leq 0.7$) were obtained as a single phase compound. They crystallize in an orthorhombic superstructure derived from that of the cubic fluorite with space group $Cmcm$. The results of the Rietveld analysis for X-ray diffraction profiles of $\text{Pr}_3(\text{Ru}_{1-x}\text{Ta}_x)\text{O}_7$ showed that Ru and Ta atoms are randomly situated at the six-coordinate $4b$ site. For $(\text{Pr}_{1-x}\text{Y}_x)_3\text{RuO}_7$, with increasing the concentration of Y ions (x value), the smaller Y ions occupy selectively the seven-coordinate $8g$ site rather than the eight-coordinate $4a$ site.

Through magnetic susceptibility measurements for $\text{Pr}_3(\text{Ru}_{1-x}\text{Ta}_x)\text{O}_7$, the antiferromagnetic transition temperatures decrease linearly with increasing x value, and at $x = 0.75$ no magnetic ordering was found down to 1.8 K, indicating the magnetic interaction is not one-dimensional, but three-dimensional. On the other hand, the antiferromagnetic transition temperature for $(\text{Pr}_{1-x}\text{Y}_x)_3\text{RuO}_7$ decreases with increasing x value, but above $x \geq 0.50$ it becomes constant (~ 12 K). This result indicates that Pr^{3+} ions at the seven-coordinate site greatly contribute to the antiferromagnetic interactions observed in $(\text{Pr}_{1-x}\text{Y}_x)_3\text{RuO}_7$.

Density functional calculations of Pr_3RuO_7 demonstrate that the electronic structure gives insulating character and that oxygen 2p orbitals hybridize strongly with Ru 4d orbitals in the valence band (VB). Near the top of VB, the Pr 4f orbitals at the seven-coordinated site also show a weak hybridization with the O(1) 2p orbitals. The Ru-O(1)-Pr superexchange pathway take part in three-dimensional magnetic interaction and play an important role in an enhancement of long-range magnetic ordering.

1. Introduction

Magnetic properties of compounds containing both rare earth and transition metal have attracted a great deal of interest, because they often show anomalous magnetic behavior due to interactions of unpaired $4f$ electrons and d electrons.

Among them, compounds of composition Ln_3MO_7 , where Ln is a rare earth and M is the $4d$ or $5d$ transition metal, have been investigated by many researchers. They have a defect-fluorite structure. The relationship to the fluorite structure is as follows. The fluorite unit cell for oxides has the composition $M^{4+}_4O_8$. If the four tetravalent metal ions are replaced by three trivalent ions (Ln) and one pentavalent ion (M), one oxide vacancy is formed per fluorite cell. Due to significant differences in radii between the Ln^{3+} and M^{5+} ions, cation ordering occurs on the metal sites and the oxide-vacancy orders on the anion sites. The M^{5+} ion is coordinated with six oxygen ions, forming an MO_6 octahedron. These octahedra share corners forming one-dimensional chains which are oriented along the c -axis.

Many studies have been performed, due to this unique crystal structure and possible related magnetic properties for Ln_3MO_7 compounds ($M = Mo$ [1-3], Ru [4-17], Re [18-21], Os [13, 22-24], and Ir [25-28]), especially for the magnetic properties of compounds containing Ru^{5+} ion at the M -site because of its largest possible spin ($S = 3/2$) among the $4d$ and $5d$ transition metals. Among many Ln_3MO_7 compounds, we focus our attention on the magnetic properties of Pr_3RuO_7 . Magnetic susceptibility and specific heat measurements show that Pr_3RuO_7 orders magnetically at 55 K [8]. This ordering temperature is the highest compared

with those for other Ln_3MO_7 compounds.

In order to clarify why Pr_3RuO_7 shows such high magnetic transition temperature, we prepared two types of solid solutions in which magnetic ions (Ru^{5+} and Pr^{3+}) are replaced by diamagnetic ions, i.e., $Pr_3(Ru_{1-x}Ta_x)O_7$ and $(Pr_{1-x}Y_x)_3RuO_7$. Through X-ray diffraction measurements, their structures were determined, and magnetic susceptibility measurements were performed from 1.8 to 400 K to study their magnetic properties. We also performed calculations of the electronic structure and the density of states (DOS) for Pr_3RuO_7 .

2. Experimental

2.1. Sample Preparation

2.1.1. $Pr_3(Ru_{1-x}Ta_x)O_7$

Solid solutions $Pr_3(Ru_{1-x}Ta_x)O_7$ ($x = 0, 0.1, 0.2, \dots, 0.9, 1.0$) were prepared by the conventional solid state reactions. As starting materials, praseodymium oxide Pr_6O_{11} , ruthenium dioxide RuO_2 , and tantalum oxide Ta_2O_5 were used. They were weighed in an appropriate metal ratio and the mixtures were ground in an agate mortar. The mixtures were pressed into pellets and then heated in air at 1300 °C for 12 h. After cooling to room temperature, the pellets were crushed, re-pressed into pellets, and reheated in the same conditions. These procedures were repeated four times with several intermediate grindings.

2.1.2. $(Pr_{1-x}Y_x)_3RuO_7$

Pr_6O_{11} , Y_2O_3 and RuO_2 were used as starting materials. After weighing these materials, they were dissolved in heated nitric acid. RuO_2 does not dissolve and remains as powders. Then, citric acid and ethylene glycol were added to this solution with a molar ratio of 5:1 against the $(Pr_{1-x}Y_x)_3RuO_7$. The precipitates were percolated and heated in air at 675°C for 12 h. After cooling to room temperature, the mixtures were ground in an agate mortar. The mixtures were pressed into pellets and then heated in air at 1300°C for 12 h.

2.2. X-ray Diffraction Analysis

Powder X-ray diffraction profiles were measured using a Rigaku Multi-Flex diffractometer with Cu- $K\alpha$ radiation ($\lambda = 1.5406 \text{ \AA}$) equipped with a curved graphite monochromator. The data were collected by step-scanning in the angle range of $10^\circ \leq 2\theta \leq 120^\circ$ at a 2θ step-size of 0.02° .

The X-ray diffraction data were analyzed by the Rietveld technique, using the programs RIETAN-FP [29], and the crystal structure was drawn by using the VESTA program [30].

2.3. Magnetic Susceptibility Measurements

The temperature-dependence of the magnetic susceptibility was measured in an applied field of 0.1T over the temperature range of $1.8\text{K} \leq T \leq 400\text{K}$, using a SQUID magnetometer (Quantum Design, MPMS5S). The susceptibility measurements were performed under both zero-field-cooled (ZFC) and field-cooled (FC) conditions. The former was measured upon heating the sample to 400 K under the applied magnetic field of 0.1 T after zero-field cooling to 1.8 K. The latter was measured upon cooling the sample from 400 to 1.8 K at 0.1 T.

2.4 DFT Calculation

Calculations of the electronic structure and the density of states (DOS) were performed using the WIEN2k program package [31]. This program employs the full-potential linearized augmented plane wave + local orbitals (FP-LAPW+lo) method based on density functional theory (DFT). We used the generalized gradient approximation (GGA) + Hubbard U parameter for the Ru 4d and the Pr 4f electrons with spin-orbit coupling (SOC). In the calculations, the convergence parameter was set to be $R_{\text{MT}}k_{\text{max}} = 7.0$, and the muffin-tin (MT) spheres are $R_{\text{MT}}(\text{Pr}) = 2.20$ bohr, $R_{\text{MT}}(\text{Ru}) = 1.96$ bohr, and $R_{\text{MT}}(\text{O}) = 1.69$ bohr. We used $10 \times 10 \times 8$ meshes with 120 k points in the first Brillouin zone (B.Z.). The U parameters of Ru 4d and Pr 4f orbitals are set to be 3.0 eV and 4.0 eV, respectively.

3. Results and Discussion

3.1. $\text{Pr}_3(\text{Ru}_{1-x}\text{Ta}_x)\text{O}_7$

For all $\text{Pr}_3(\text{Ru}_{1-x}\text{Ta}_x)\text{O}_7$ ($x = 0, 0.1, 0.2, \dots, 0.9, 1.0$), single-phase compounds were obtained. Figure 1 (a) shows the X-ray diffraction profile of $\text{Pr}_3(\text{Ru}_{0.5}\text{Ta}_{0.5})\text{O}_7$. The diffraction patterns are similar to that for the fluorite structure and all reflections appeared to be consistent with the C -centered conditions, $h + k = 2n$, and $h\ 0\ l$ reflections with odd l are absent. We have analyzed the X-ray diffraction profiles with the space group $Cmcm$, which is the same space group as those for end members Pr_3RuO_7 [8] and Pr_3TaO_7 [32]. All the reflections observed could be successfully indexed. The crystallographic data determined for $\text{Pr}_3(\text{Ru}_{0.5}\text{Ta}_{0.5})\text{O}_7$ are listed in Table 1.

Complete solid solutions are formed for $\text{Pr}_3(\text{Ru}_{1-x}\text{Ta}_x)\text{O}_7$. The results of the Rietveld analysis for the X-ray diffraction profiles showed that Ru and Ta atoms are randomly situated at the $4b$ site. Figure 2 shows the crystal structure of Pr_3MO_7 ($M = \text{Ru}_{0.5}\text{Ta}_{0.5}$). The MO_6 octahedra share the O(3) ions, forming a one-dimensional zig-zag chain parallel to the [001] direction. There are two types of oxygen coordination around Pr ions. One-third of the Pr ions, Pr(1) are coordinated by eight oxygen ions and the Pr(1)O_8 cubes also form a one-dimensional chain through edge-sharing. The MO_6 and Pr(1)O_8 chains lie alternately parallel to the (100) plane, and the rest of the Pr ions, Pr(2) are seven-coordinated by oxygen ions between the slabs consisting of these chains.

Figure 3 shows the variation of lattice parameters for $\text{Pr}_3(\text{Ru}_{1-x}\text{Ta}_x)\text{O}_7$ against x values. With increasing substitution of tantalum for ruthenium, the lattice parameters b and c increase, which is due to larger ionic radius of tantalum compared with that of ruthenium. As seen in Fig. 2, Pr(1)O_8 cubes share edges with neighboring Pr(1)O_8 cubes and MO_6 octahedra. The substitution of Ta for Ru directly affects the expansion of the b - c plane of the lattice. On the other hand, the lattice parameter a does not change with x values. This result is easily understandable from Fig. 2, that is, because of the large space between the slabs consisting of Pr(1)O_8 and MO_6 , the expansion of MO_6 octahedra due to Ta-substitution for Ru does not affect the lattice in the direction of a -axis.

Figure 4 depicts the temperature dependence of the magnetic susceptibility for $\text{Pr}_3(\text{Ru}_{1-x}\text{Ta}_x)\text{O}_7$ ($x = 0.0, 0.25, 0.50, 0.75$) in the temperature range between 1.8 and 200 K. Pr_3RuO_7 shows a clear antiferromagnetic ordering at 55 K. Figure 5 depicts the variation of

Néel temperatures (T_N) for $\text{Pr}_3(\text{Ru}_{1-x}\text{Ta}_x)\text{O}_7$ with x values. With increasing substitution of Ta for Ru (x value), the antiferromagnetic transition temperature decreases linearly. Compounds with $x \leq 0.70$ show the antiferromagnetic transition at low temperatures, and no magnetic ordering was observed for compounds with $x \geq 0.75$. Considering the crystal structure of $\text{Pr}_3(\text{Ru}_{1-x}\text{Ta}_x)\text{O}_7$, low-dimensional magnetic properties are expected to be observed. Theoretical studies predict that the critical concentration of magnetic ions ($c = 1-x$) below which the magnetic ordering disappears should be above $c = 0.5$ for low-dimensional matters [33]. However, as shown in Fig. 5, experimental results are that compounds $\text{Pr}_3(\text{Ru}_{1-x}\text{Ta}_x)\text{O}_7$ with $x \geq 0.50$ ($c \leq 0.50$) still show an antiferromagnetic ordering at low temperatures. These results indicate that the magnetic interactions observed in $\text{Pr}_3(\text{Ru}_{1-x}\text{Ta}_x)\text{O}_7$ are three-dimensional. The results of the calculations of the electronic structure and the density of states (DOS) for Pr_3RuO_7 , as will be described later, also show that the magnetic interactions are three-dimensional.

Figure 6 shows the reciprocal magnetic susceptibility vs. temperature curve for $\text{Pr}_3(\text{Ru}_{0.5}\text{Ta}_{0.5})\text{O}_7$. In the high temperature region, the Curie-Weiss law fitting was applied to the temperature dependence of the susceptibility. The effective magnetic moment and the Weiss constant for $\text{Pr}_3(\text{Ru}_{0.5}\text{Ta}_{0.5})\text{O}_7$ were obtained to be $5.98 \mu_B$ and 13 K, respectively. Table 2 lists the effective magnetic moment (μ_{eff}) and the Weiss constant (θ) for $\text{Pr}_3(\text{Ru}_{1-x}\text{Ta}_x)\text{O}_7$. Since both Pr^{3+} and Ru^{5+} ions contribute to the paramagnetic behavior of $\text{Pr}_3(\text{Ru}_{1-x}\text{Ta}_x)\text{O}_7$, its effective magnetic moment should be calculated from the equation $\mu_{\text{calc}} = \sqrt{3\mu_{\text{Pr}^{3+}}^2 + (1-x)\mu_{\text{Ru}^{5+}}^2}$. Although the effective magnetic moment for the free Pr^{3+} ion is 3.58

μ_B , that for the Pr^{3+} ion in Pr_3TaO_7 is experimentally obtained to be $3.09 \mu_B$. This result means that the smaller effective magnetic moment of Pr^{3+} ion is due to the effect of crystal field [32]. Similar results have been reported for other Pr_3MO_7 ($M = \text{Nb}, \text{Sb}$) [34, 35]. Using the effective magnetic moment obtained experimentally for $\text{Pr}_3(\text{Ru}_{1-x}\text{Ta}_x)\text{O}_7$ and the moment of Pr^{3+} , the magnetic moments of Ru^{5+} in $\text{Pr}_3(\text{Ru}_{1-x}\text{Ta}_x)\text{O}_7$ are estimated. They are also listed in Table 2, and are in the range of $3.6 \sim 3.9 \mu_B$, which agrees with the moment of Ru^{5+} (the electronic configuration is $[\text{Kr}]4d^3$).

3.2. $(\text{Pr}_{1-x}\text{Y}_x)_3\text{RuO}_7$

It has been reported that Ln_3RuO_7 compounds are formed for $\text{Ln} = \text{La} \sim \text{Dy}$ [4-17]. For rare earth smaller than Dy, Ln_3RuO_7 has not been prepared, i.e., Y_3RuO_7 has not been obtained. In this study, single-phase compounds were obtained for $(\text{Pr}_{1-x}\text{Y}_x)_3\text{RuO}_7$ solid solutions with $x = 0.1, 0.2, \dots, 0.7$. Figure 1 (b) shows the X-ray diffraction profile of $(\text{Pr}_{0.7}\text{Y}_{0.3})_3\text{RuO}_7$. All the X-ray diffraction reflections are analyzed with the space group $Cmcm$. In the structure of Ln_3RuO_7 , there are two kinds of oxygen-coordination environment around Ln ions. One-third of the Ln ions are situated in the eight-coordination and the remaining two-third of the Ln ions are seven-coordinated. When different Ln' and Ln'' ions are incorporated into Ln sites of Ln_3RuO_7 , we may expect to observe that the larger Ln' ions sit selectively at the eight-coordination site and that the smaller Ln'' ions are located at the seven-coordinate site. Due to large difference in atomic numbers between Pr and Y, it is possible to distinguish them by powder X-ray diffraction measurements. We analyzed the

X-ray diffraction data for $(\text{Pr}_{1-x}\text{Y}_x)_3\text{RuO}_7$ with space group $Cmcm$. The crystallographic data determined for $(\text{Pr}_{0.7}\text{Y}_{0.3})_3\text{RuO}_7$ are listed in Table 3.

Table 4 summaries the lattice parameters and occupancy by Y ions at the seven-coordinate 8g site for $(\text{Pr}_{1-x}\text{Y}_x)_3\text{RuO}_7$. Figure 7 shows the occupancy by the Y ions at the seven-coordinate 8g site and the eight-coordinate 4a site against the x value. With increasing the concentration of Y ions (x value), the occupancy of Y ions at the 8g site increases and that at the 4a site greatly decreases, i.e., the smaller Y ions occupy the seven-coordinate 8g site rather than the eight-coordinate 4a site.

Figure 8 shows the variation of lattice parameters for $(\text{Pr}_{1-x}\text{Y}_x)_3\text{RuO}_7$ against x value. With increasing substitution of yttrium for praseodymium, all the lattice parameters a , b and c decrease, which is due to smaller ionic radius of yttrium than that of praseodymium. As seen in Fig. 8, it is clear that the decrease of lattice parameter a with increasing x value is more rapid than those of lattice parameters b and c . This result reflects the fact that smaller Y ions compared with the Pr ions preferentially occupy the seven-coordinated 8g sites which are situated between the slabs consisting of PrO_8 and RuO_6 chains (see Fig.2).

Figure 9 depicts the temperature dependence of the magnetic susceptibility for $(\text{Pr}_{1-x}\text{Y}_x)_3\text{RuO}_7$ ($x = 0.0, 0.3, 0.6$) in the temperature range between 1.8 and 200 K. All the compounds obtained as a single-phase show an antiferromagnetic ordering at low temperatures. Figure 10 depicts the variation of Néel temperatures (T_N) for $(\text{Pr}_{1-x}\text{Y}_x)_3\text{RuO}_7$ with x value. The data for $(\text{Pr}_{1-x}\text{La}_x)_3\text{RuO}_7$ solid solutions are also plotted in the same figure [36]. With increasing the substitution of Y for Pr (x value), the antiferromagnetic transition temperature

decreases considerably. Above $x \geq 0.50$, the Néel temperature for $(\text{Pr}_{1-x}\text{Y}_x)_3\text{RuO}_7$ is almost constant (~ 12 K). These behaviors are quite different from those observed for $(\text{Pr}_{1-x}\text{La}_x)_3\text{RuO}_7$. In $(\text{Pr}_{1-x}\text{La}_x)_3\text{RuO}_7$, Pr and La ions are randomly distributed at the $4a$ and $8g$ sites, because the ionic radius of La^{3+} is comparable to that of Pr^{3+} . The Néel temperature decreases linearly with the substitution of La for Pr. The large decrease of Néel temperatures for $(\text{Pr}_{1-x}\text{Y}_x)_3\text{RuO}_7$ should be ascribed to the fact that nonmagnetic Y^{3+} ions are preferentially at the seven-coordinate $8g$ site. This result means that the Pr ions at the seven-coordinate site greatly contribute to the antiferromagnetic ordering of Pr_3RuO_7 .

In the paramagnetic temperature region, the Curie-Weiss law fitting was applied to the temperature dependence of the susceptibility, and the effective magnetic moment and the Weiss constant for $(\text{Pr}_{1-x}\text{Y}_x)_3\text{RuO}_7$ were obtained. They are listed in Table 5. The effective magnetic moment for $(\text{Pr}_{1-x}\text{Y}_x)_3\text{RuO}_7$ should be calculated from the equation $\mu_{\text{calc}} = \sqrt{3(1-x)\mu_{\text{Pr}^{3+}}^2 + \mu_{\text{Ru}^{5+}}^2}$. Using the effective magnetic moment obtained experimentally for $(\text{Pr}_{1-x}\text{Y}_x)_3\text{RuO}_7$ and the moment of Pr^{3+} , the magnetic moments of Ru^{5+} in $(\text{Pr}_{1-x}\text{Y}_x)_3\text{RuO}_7$ are estimated. They are also listed in Table 5, and are in the range of $3.6 \sim 3.7 \mu_{\text{B}}$, which agrees with the moment of Ru^{5+} .

3.3 DFT Calculation

In order to discuss the electronic properties, we carried out the GGA + U calculation with SOC. In the DFT + U calculation, the band structure is sensitive to the Slater-Kanamori interaction parameters U and J . In the case of ruthenates, the effective Coulomb interactions

$U_{\text{eff}} (= U - J)$ of Ru 4d were often used in the range of ~ 2 to ~ 4 eV [37-40]. The U parameters of trivalent rare earth 4f electrons were calculated through the DFT + U calculations for Ln_2O_3 ($Ln = \text{La-Lu}$), and U of Pr 4f was estimated to be about 4 eV [41]. Thus, we have adopted 3.0 eV for Ru 4d and 4.0 eV for Pr 4f as the U_{eff} parameter.

Figure 11(a) displays the total densities of states (DOS) and the partial DOS of total electrons of Pr, Ru, and O for Pr_3RuO_7 . The enlargement plot for the partial DOS of Ru and its surrounding O(1) and O(3) ions is shown in Fig. 11(b). The occupied and unoccupied bands form a band gap of 0.6 eV around the Fermi level. The valence band (VB) demonstrates a strong hybridization between the Ru 4d orbitals and the O(1), (3) 2p orbitals and the $pd\sigma$ and $pd\pi$ bonding-antibonding nature in RuO_6 octahedra in the broad range from -8 to 0 eV. The Ru moment is estimated to be $1.81 \mu_B$ and is greatly smaller than the $4d^3$ spin-only value. The major reduction in the Ru moment appears to result from hybridization, and the surrounding oxygen ions also exhibit spin polarization ($0.12\sim 0.14 \mu_B$). This polarization spreads over RuO_6 and forms effective magnetic cluster with the total spin moment of $\sim 2.6 \mu_B$, and this value is slightly smaller than the theoretical one ($3 \mu_B$). The bottom of conduction band (CB) mainly consists of down-spin Ru 4d and O(1), (3) 2p orbitals. This distribution of Ru 4d and O 2p orbitals in VB and CB is similar to that in the electronic structure of the double perovskite Sr_2YRuO_6 containing RuO_6 octahedra [42]. The energy levels for Pr_3RuO_7 indicate that this compound is classified in a Mott-Hubbard insulator [43].

The up-spin Pr(1) and (2) 4f orbitals with spin moments of $\sim 1.91 \mu_B$ coexist near the top of VB, and the Pr(2) 4f orbitals also show a weak hybridization with the O(1) 2p orbitals. For

O(2) bonding with only Pr ions, the O(2) 2p orbitals are located from -4 to -1 eV in VB, and the hybridization with the Pr 4f orbitals is negligible in comparison with that of O(1) 2p orbitals. The spin densities and the spin polarization of Pr₃RuO₇ are shown in Fig. 12. Significant spin polarization is seen on the magnetic Pr and Ru ions but there is also some on the O(1), (3) ligands of Ru. The Néel temperature T_N (~ 55 K) of Pr₃RuO₇ is considerably higher than those (T_N ~ 15-23 K) of the other Ln₃RuO₇ compounds [4-17]. For these compounds except for Pr₃RuO₇, one-dimensional Ru-O(3)-Ru superexchange interaction is predicted to be strong in one dimensional chain consisting of corner-sharing RuO₆, and three-dimensional long-range magnetic ordering should occur via the Ru-O(1)-O(1)-Ru super-superexchange interaction. On the other hand, the contribution of Ln 4f orbitals to a long-range magnetic ordering is considered to be small because of low T_N . In the case of Pr₃RuO₇, because the Ru-O hybridized orbital and the up-spin Pr 4f orbital overlap just below the Fermi level, the Ru-O(1)-Pr superexchange interactions take part in three-dimensional magnetic interaction and play an important role in an enhancement of long-range magnetic ordering.

Summary

Solid solutions Pr₃(Ru_{1-x}Ta_x)O₇ ($0 \leq x \leq 1.0$) and (Pr_{1-x}Y_x)₃RuO₇ ($0 \leq x \leq 0.7$) were obtained as a single phase compound. The Rietveld analysis for X-ray diffraction profiles of Pr₃(Ru_{1-x}Ta_x)O₇ showed that Ru and Ta atoms are randomly situated at the six-coordinate 4b site. For (Pr_{1-x}Y_x)₃RuO₇, the smaller Y ions occupy mostly the seven-coordinate 8g site rather than the eight-coordinate 4a site. The change of the Néel temperatures for Pr₃(Ru_{1-x}Ta_x)O₇

with x value indicates that the magnetic interactions between Ru^{5+} ions are three-dimensional.

References

- [1] J. E. Greedan, N. P. Raju, A. Wegner, P. Gougeon, and J. Padiou, *J. Solid State Chem.*, **129**, 320-327 (1997).
- [2] H. Nishimine, M. Wakeshima, and Y. Hinatsu, *J. Solid State Chem.*, **178**, 1221-1229 (2005).
- [3] M. Wakeshima and Y. Hinatsu, *J. Solid State Chem.*, **183**, 2681-2688 (2010).
- [4] F. P. F. van Berkel and D. J. W. IJdo, *Mater. Res. Bull.*, **21**, 1103-1106 (1986).
- [5] W. A. Groen, F. P. F. van Berkel, and D. J. W. IJdo, *Acta Crystallogr. Sec. C* **43**, 2262-2264 (1986).
- [6] A. Kahn-Harari, L. Mazerrolles, D. Michel, and F. Robert, *J. Solid State Chem.*, **116**, 103-106 (1995).
- [7] P. Khalifah, R. W. Erwin, J. W. Lynn, Q. Huang, B. Batlogg, and R. J. Cava, *Phys. Rev.*, **B 60**, 9573-9578 (1999).
- [8] F. Wiss, N. P. Raju, A. S. Wills, and J. E. Greedan, *Inter. J. Inorg. Mater.*, **2**, 53-59 (2000).
- [9] B.P.Bontchev, A.J.Jacobson, M.M.Gospodinov, V. Skumryev, V. N. Popov, B. Lorenz, R. L. Meng, A. P. Litvinchuk, and M.N. Iliev, *Phys. Rev.* **B. 62**, 12235-12240 (2000).
- [10] D. Harada and Y. Hinatsu, *J. Solid State Chem.*, **158**, 245-253 (2001).
- [11] D. Harada, Y. Hinatsu, and Y. Ishii, *J. Phys.: Condens. Matter*, **13**, 10825-10836 (2001).
- [12] D. Harada and Y. Hinatsu, *J. Solid State Chem.*, **164**, 163-168 (2002).
- [13] R. Lam, F. Wiss, and J. E. Greedan, *J. Solid State Chem.* **167**, 182-187 (2002).

- [14] W. R. Gemmill, M. D. Smith, and H-C, zur Loye, *Inorg. Chem.*, **43**, 4254-4261 (2004).
- [15] N. Ishizawa, K. Hiraga, D. du Boulay, H. Hibino, T. Ida, and S. Oishi, *Acta Cryst.*, **E62**, i13-i16 (2006).
- [16] Y. Hinatsu and Y. Doi, *J. Solid State Chem.*, **220**, 22-27 (2014).
- [17] Y. Hinatsu and Y. Doi, *J. Solid State Chem.*, **239**, 214-219 (2016).
- [18] G. Wltschek, H. Paulus, I. Svoboda, H. Ehrenberg, and H. Fuess, *J. Solid State Chem.* **125**, 1-4 (1996).
- [19] R. Lam, T. Langet, and J. E. Greedan, *J. Solid State Chem.* **171**, 317-323 (2002).
- [20] Y. Hinatsu, M. Wakeshima, N. Kawabuchi, and N. Taira, *J. Alloys Compd.*, **374**, 79-83 (2004).
- [21] M. Wakeshima and Y. Hinatsu, *J. Solid State Chem.*, **179**, 3575-3581 (2006).
- [22] J. R. Plaisier, R. J. Drost, and D. J. W. IJdo, *J. Solid State Chem.* **169**, 189-198 (2002).
- [23] W. R. Gemmill, M. D. Smith, Y. A. Mozharivsky, G. J. Miller, and H-C, zur Loye, *Inorg. Chem.*, **44**, 7047-7055 (2005).
- [24] Y. Hinatsu and Y. Doi, *J. Solid State Chem.*, **198**, 176-185 (2013).
- [25] J. F. Vente and D. J. W. IJdo, *Mater. Res. Bull.*, **26**, 1255-1262 (1991).
- [26] T. Fennell, S. T. Bramwell, and M. A. Green, *Can. J. Phys.*, **79**, 1415-1419 (2001).
- [27] H. Nishimine, M. Wakeshima, and Y. Hinatsu, *J. Solid State Chem.*, **177**, 739-744 (2004).
- [28] Y. Hinatsu, Y. Doi, H. Nishimine, M. Wakeshima, and M. Sato, *J. Alloys Compd.*, **488**, 541-545 (2009).
- [29] F. Izumi and K. Momma, *Solid State Phenom.*, **130**, 15-20 (2007).

- [30] K. Momma and F. Izumi, *Appl. Crystallogr.*, **41**, 653-658 (2008).
- [31] P. Blaha, K. Schwarz, G. Madsen, D. Kvasnicka and J. Luitz, WIEN2k, An Augmented Plane Wave + Local Orbitals Program for Calculating Crystal Properties (Karlheinz Schwarz, Techn. Universität Wien, Austria), 2001. ISBN 3-9501031-1-2.
- [32] M. Wakeshima, H. Nishimine, and Y. Hinatsu, *J. Phys.: Condens. Matter*, **16**, 4103-4120 (2004).
- [33] L.J. de Jongh, "Magnetic Properties of Layered Transition Metal Compounds", Kluwer Academic, Dordrecht, 1990.
- [34] J. F. Vente, R. B. Helmholdt, and D. J. W. IJdo, *J. Solid State Chem.*, **108**, 18-23 (1994).
- [35] Y. Doi, Y. Harada, and Y. Hinatsu, *J. Solid State Chem.*, **182**, 709-715 (2009).
- [36] Z. X. Zhou, G. Cao, S. McCall, J. E. Crow, R. P. Guertin, C. H. Mielke, and D. G. Rickel, *Philosophical Magazine*, **82**, 1401-1412 (2002).
- [37] H.-T. Jeng, S.-H. Lin, and C.-S. Hsue, *Phys. Rev. Lett.*, **97**, 067002 (2006).
- [38] J. Mravlje, M. Aichhorn, T. Miyake, K. Haule, G. Kotliar, and A. Georges, *Phys. Rev. Lett.*, **106**, 096401 (2011).
- [39] H. T. Dang, J. Mravlje, A. Georges, and A. J. Millis, *Phys. Rev. Lett.*, **115**, 107003 (2015).
- [40] X. Deng, K. Haule, and G. Kotliar, *Phys. Rev. Lett.*, **116**, 256401 (2016).
- [41] B. Huang, *J. Comput. Chem.*, **37**, 825-835 (2016).
- [42] I. I. Mazin and D. J. Singh, *Phys. Rev. B*, **56**, 2556-2570 (1997).
- [43] M. Imada, A. Fujimori, Y. Tokura, *Rev. Mod. Phys.* **70**, 1039-1263 (1998).

Figure captions

Fig. 1 Powder x-ray diffraction profiles for (a) $\text{Pr}_3(\text{Ru}_{0.5}\text{Ta}_{0.5})\text{O}_7$ and (b) $(\text{Pr}_{0.7}\text{Y}_{0.3})_3\text{RuO}_7$.

The calculated and observed profiles are shown on the top solid line and cross markers, respectively. The vertical marks in the middle show positions calculated for Bragg reflections. The lower trace is a plot of the difference between calculated and observed intensities.

Fig. 2. Schematic crystal structure of Pr_3MO_7 ($M = \text{Ru}_{0.5}\text{Ta}_{0.5}$). The lower left and right figures are the structures viewed from the [100] direction and [010] direction, respectively.

Fig. 3. Variation of lattice parameters for $\text{Pr}_3(\text{Ru}_{1-x}\text{Ta}_x)\text{O}_7$ with x value.

Fig. 4. Temperature dependence of magnetic susceptibility for $\text{Pr}_3(\text{Ru}_{1-x}\text{Ta}_x)\text{O}_7$ in the temperature range between 1.8 and 200 K. Closed and open circles are ZFC and FC susceptibility data, respectively.

Fig. 5. Variation of Néel temperatures for $\text{Pr}_3(\text{Ru}_{1-x}\text{Ta}_x)\text{O}_7$ with x value.

Fig. 6. Temperature dependence of the reciprocal magnetic susceptibility for $\text{Pr}_3(\text{Ru}_{0.5}\text{Ta}_{0.5})\text{O}_7$ in the temperature range between 1.8 and 300 K.

Fig. 7. Occupancy by Y ions at the seven-coordinate 8g site and the eight-coordinate 4a site against x value.

Fig. 8. Variation of lattice parameters for $(\text{Pr}_{1-x}\text{Y}_x)_3\text{RuO}_7$ with x value.

Fig. 9. Temperature dependence of magnetic susceptibility for $(\text{Pr}_{1-x}\text{Y}_x)_3\text{RuO}_7$ in the temperature range between 1.8 and 200 K. Closed and open circles are ZFC and FC susceptibility data, respectively.

Fig.10. Variation of Néel temperatures for $(\text{Pr}_{1-x}\text{Y}_x)_3\text{RuO}_7$ and $(\text{Pr}_{1-x}\text{La}_x)_3\text{RuO}_7$ with x value.

Fig. 11 (a) Total densities of states (DOS) and the partial DOS of total electrons of Pr, Ru, and O for Pr_3RuO_7 . (b) Enlargement plot for the partial DOS of Ru, O(1), and O(3). The zero energy is placed at the highest occupied state.

Fig. 12 Spin density distributions in a unit cell for Pr_3RuO_7 visualized by VESTA [30].

Table 1. Structural parameters for $\text{Pr}_3(\text{Ru}_{0.5}\text{Ta}_{0.5})\text{O}_7$.

Atom	Site	occupancy	x	y	z	$B / \text{\AA}^2$
Pr(1)	$4a$	1.0	0	0	0	0.59(3)
Pr(2)	$8g$	1.0	0.225(8)	0.303(1)	1/4	0.59
Ru/Ta	$4b$	0.5/0.5	0	1/2	0	0.13
O(1)	$16h$	1.0	0.121(7)	0.316(7)	-0.038(8)	1.0
O(2)	$8g$	1.0	0.135(4)	0.025(8)	1/4	1.0
O(3)	$4c$	1.0	0	0.439(5)	1/4	1.0

Note. Space group $Cmcm$; $a = 10.9835(3) \text{\AA}$, $b = 7.4673(6) \text{\AA}$, $c = 7.6227(5) \text{\AA}$,

$V = 625.20(3) \text{\AA}^3$, $R_{\text{wp}} = 12.72 \%$, $R_{\text{B}} = 2.61 \%$, and $R_{\text{e}} = 9.93 \%$, where

$$R_{\text{wp}} = \left[\frac{\sum_i w_i (y_i - f_i(\mathbf{x}))^2}{\sum_i w_i y_i^2} \right]^{1/2}, \quad R_{\text{B}} = \frac{\sum_K |I_{\text{O}}(\mathbf{h}_K) - I(\mathbf{h}_K)|}{\sum_K I_{\text{O}}(\mathbf{h}_K)}, \text{ and}$$

$$R_{\text{e}} = \left[(N - P) / \sum_i w_i y_i^2 \right]^{1/2}.$$

Table 2. Effective magnetic moments (μ_{eff}) and Weiss constants (θ) for $\text{Pr}_3(\text{Ru}_{1-x}\text{Ta}_x)\text{O}_7$, and estimated magnetic moments for Ru^{5+} ($\mu(\text{Ru}^{5+})$).

x	$\mu_{\text{eff}} / \mu_{\text{B}}$	θ / K	$\mu(\text{Ru}^{5+}) / \mu_{\text{B}}$
0	6.43	38.5	3.56
0.1	6.44	32.8	3.79
0.2	6.24	31.6	3.61
0.3	6.14	26.1	3.62
0.4	6.01	18.9	3.54
0.5	5.98	13.0	3.78
0.6	5.85	7.40	3.77
0.7	5.76	0.51	3.88
0.8	5.59	-7.36	3.59
0.9	5.50	-17.0	3.91
1.0	5.35	-21.4	-

Table 3. Structural parameters for $(\text{Pr}_{0.7}\text{Y}_{0.3})_3\text{RuO}_7$.

Atom	Site	occupancy	x	y	z	$B/\text{\AA}^2$
Pr(1)/Y(1)	$4a$	0.81(2)/0.19	0	0	0	0.61(4)
Pr(2)/Y(2)	$8g$	0.64/0.36	0.223(7)	0.306(1)	1/4	0.61
Ru	$4b$	1.0	0	1/2	0	0.21(7)
O(1)	$16h$	1.0	0.123(4)	0.321(3)	-0.039(1)	0.40(6)
O(2)	$8g$	1.0	0.137(1)	0.027(6)	1/4	0.40
O(3)	$4c$	1.0	0	0.422(7)	1/4	0.40

Note. Space group $Cmcm$; $a = 10.7717(6)$ \AA, $b = 7.3621(2)$ \AA, $c = 7.4722(5)$ \AA,

$V = 592.57(4)$ \AA³, $R_{\text{wp}} = 13.69$ %, $R_{\text{B}} = 2.85$ %, and $R_{\text{e}} = 12.35$ %, where

$$R_{\text{wp}} = \left[\frac{\sum_i w_i (y_i - f_i(\mathbf{x}))^2}{\sum_i w_i y_i^2} \right]^{1/2}, \quad R_{\text{B}} = \frac{\sum_K |I_{\text{O}}(\mathbf{h}_K) - I(\mathbf{h}_K)|}{\sum_K I_{\text{O}}(\mathbf{h}_K)}, \text{ and}$$

$$R_{\text{e}} = \left[\frac{(N - P)}{\sum_i w_i y_i^2} \right]^{1/2}.$$

Table 4. Lattice parameters for $(\text{Pr}_{1-x}\text{Y}_x)_3\text{RuO}_7$ and occupancy by Y at the 8g site.

x	$a/\text{\AA}$	$b/\text{\AA}$	$c/\text{\AA}$	occupancy by Y at the 8g site
0	10.9830(4)	7.3803(3)	7.5309(8)	0
0.1	10.9100(7)	7.3761(5)	7.5122(4)	0.09(1)
0.2	10.8348(9)	7.3699(5)	7.4907(5)	0.22(1)
0.3	10.7717(6)	7.3621(2)	7.4722(5)	0.36(6)
0.4	10.7211(8)	7.3539(4)	7.4570(5)	0.47(7)
0.5	10.6688(9)	7.3469(3)	7.4385(4)	0.59(1)
0.6	10.6302(1)	7.3423(8)	7.4241(9)	0.69(5)
0.7	10.5772(7)	7.3299(3)	7.3996(6)	0.79(2)

Table 5. Effective magnetic moments (μ_{eff}) and Weiss constants (θ) for $(\text{Pr}_{1-x}\text{Y}_x)_3\text{RuO}_7$, and estimated magnetic moments for Ru^{5+} ($\mu(\text{Ru}^{5+})$).

x	$\mu_{\text{eff}} / \mu_{\text{B}}$	θ / K	$\mu(\text{Ru}^{5+}) / \mu_{\text{B}}$
0	6.43	38.5	3.56
0.1	6.24	30.32	3.63
0.2	5.88	24.6	3.52
0.3	5.77	13.8	3.64
0.4	5.37	5.5	3.56
0.5	5.31	-1.5	3.72
0.6	4.96	-11.3	3.63
0.7	4.73	-21.8	3.72

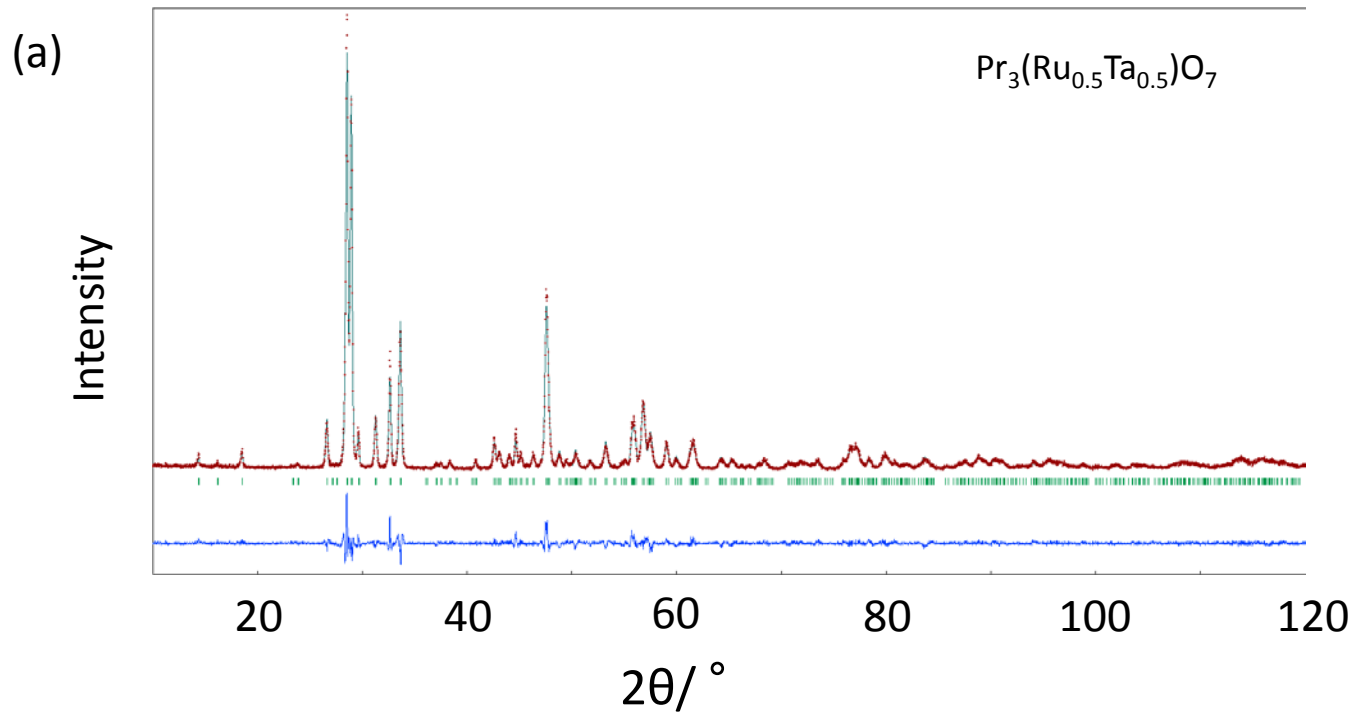


Fig.1(a)

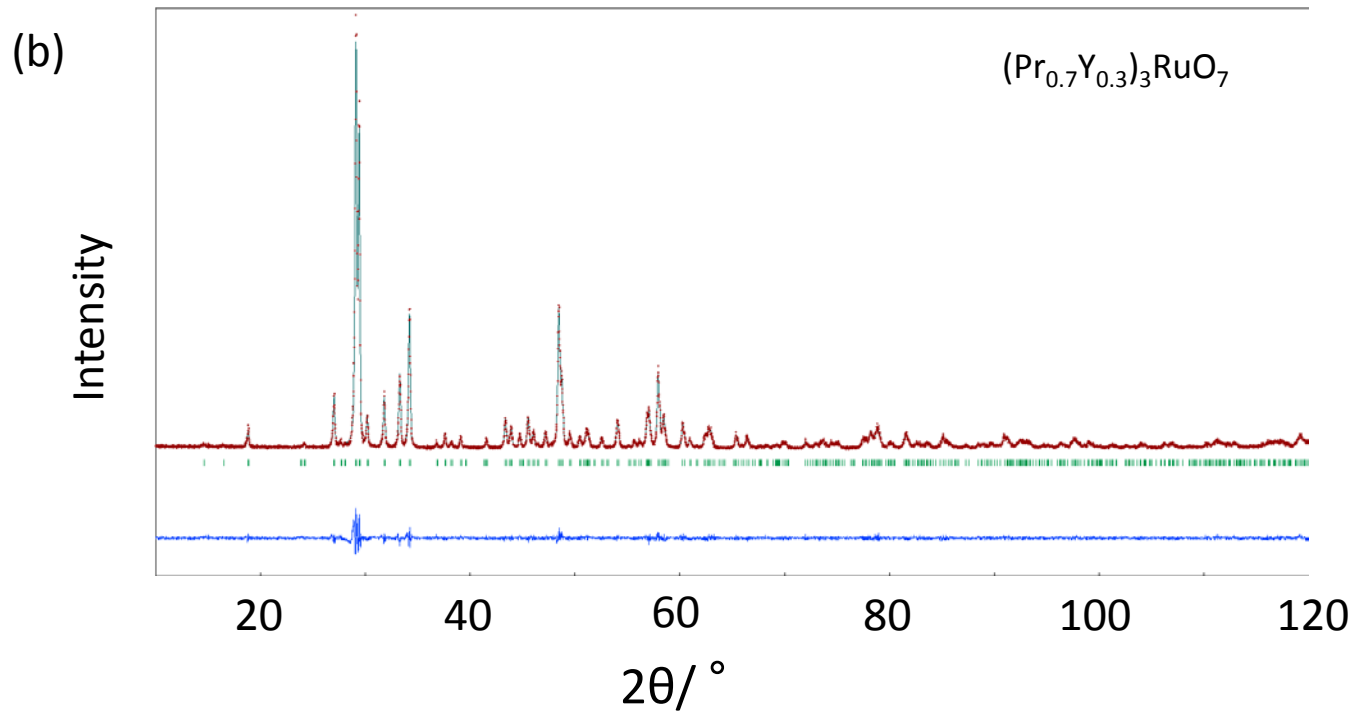


Fig.1(b)

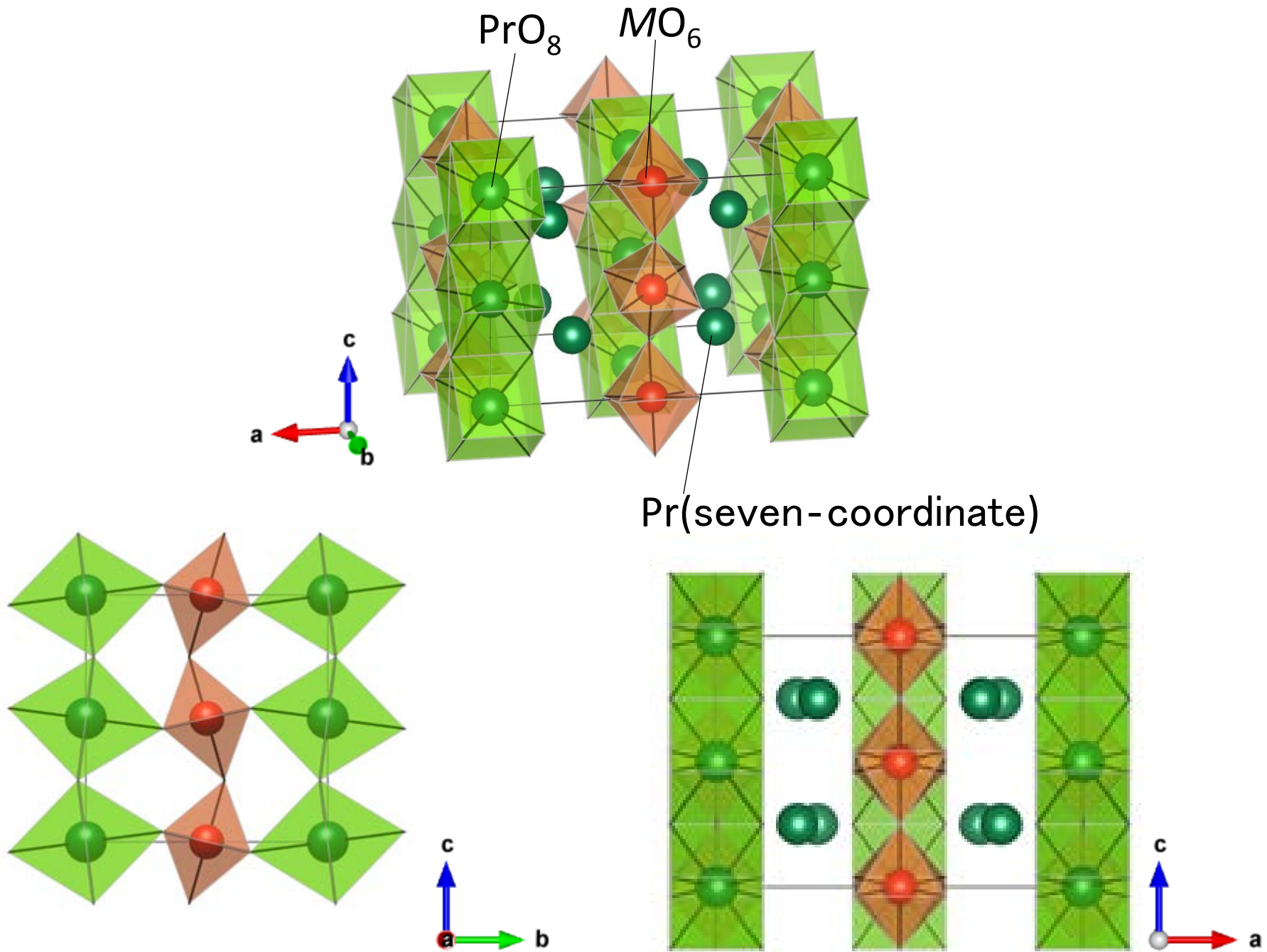


Fig.2

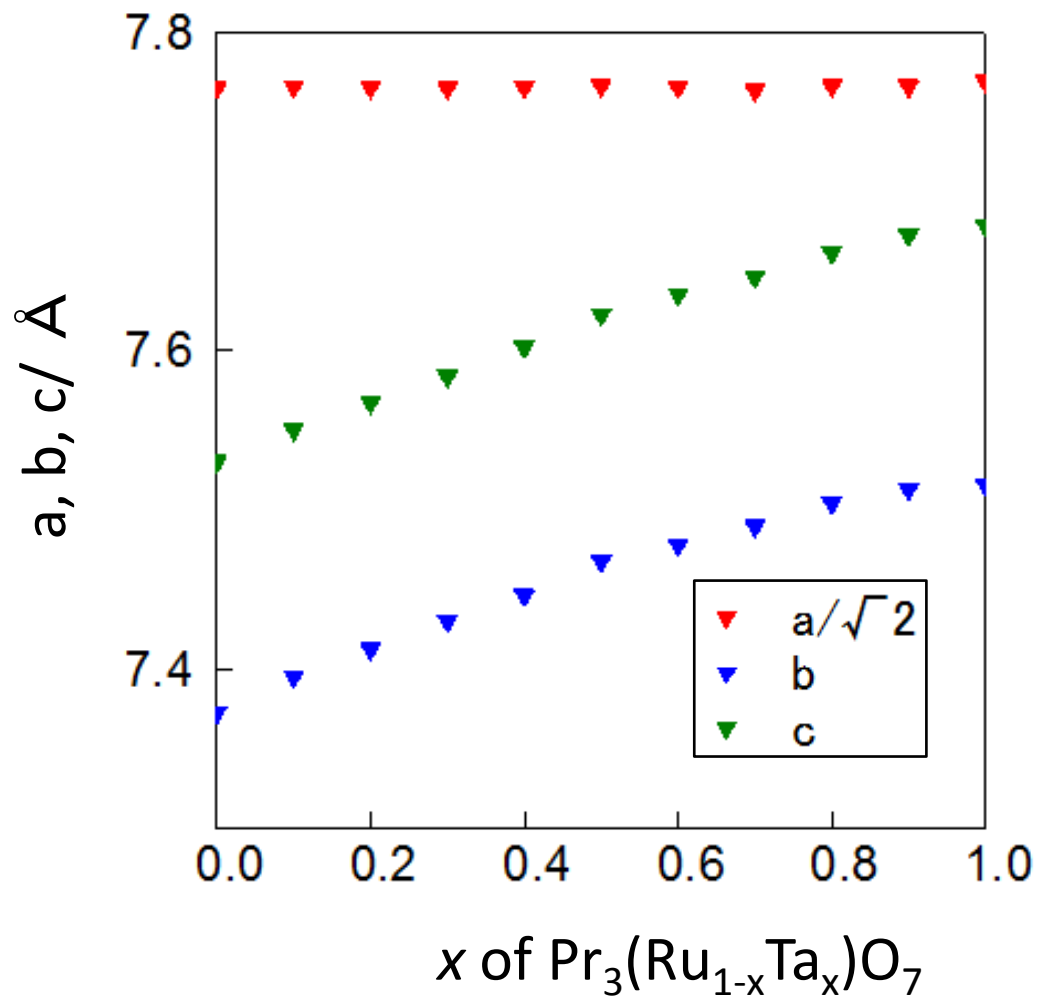


Fig.3

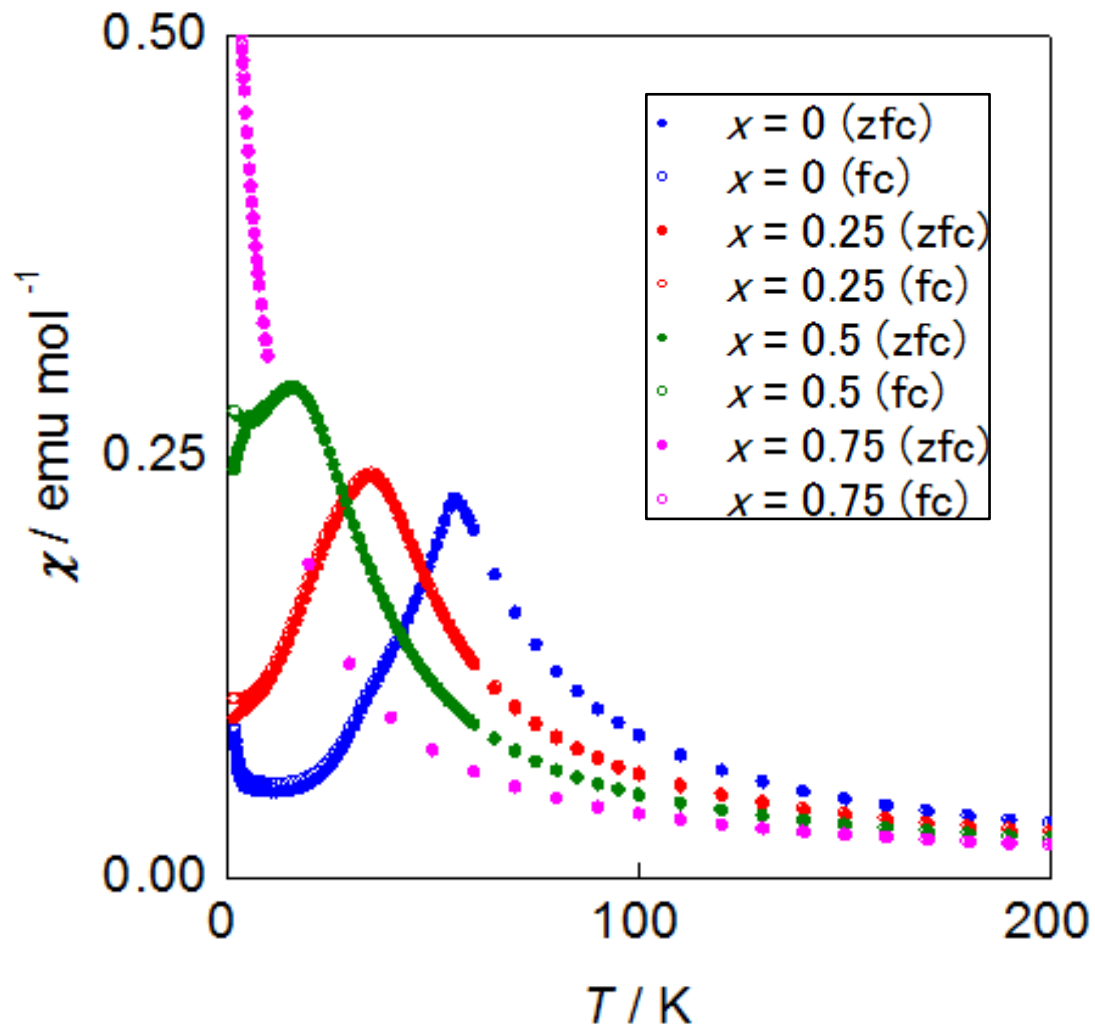


Fig.4

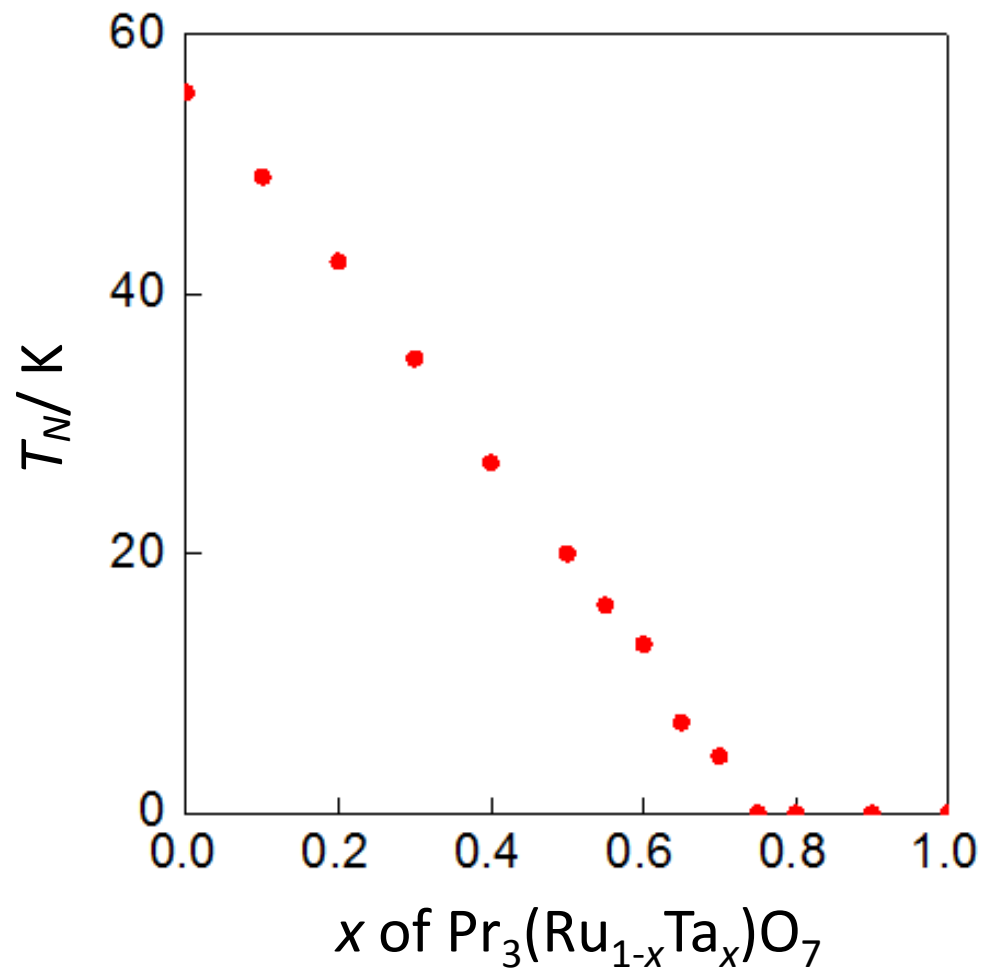


Fig.5

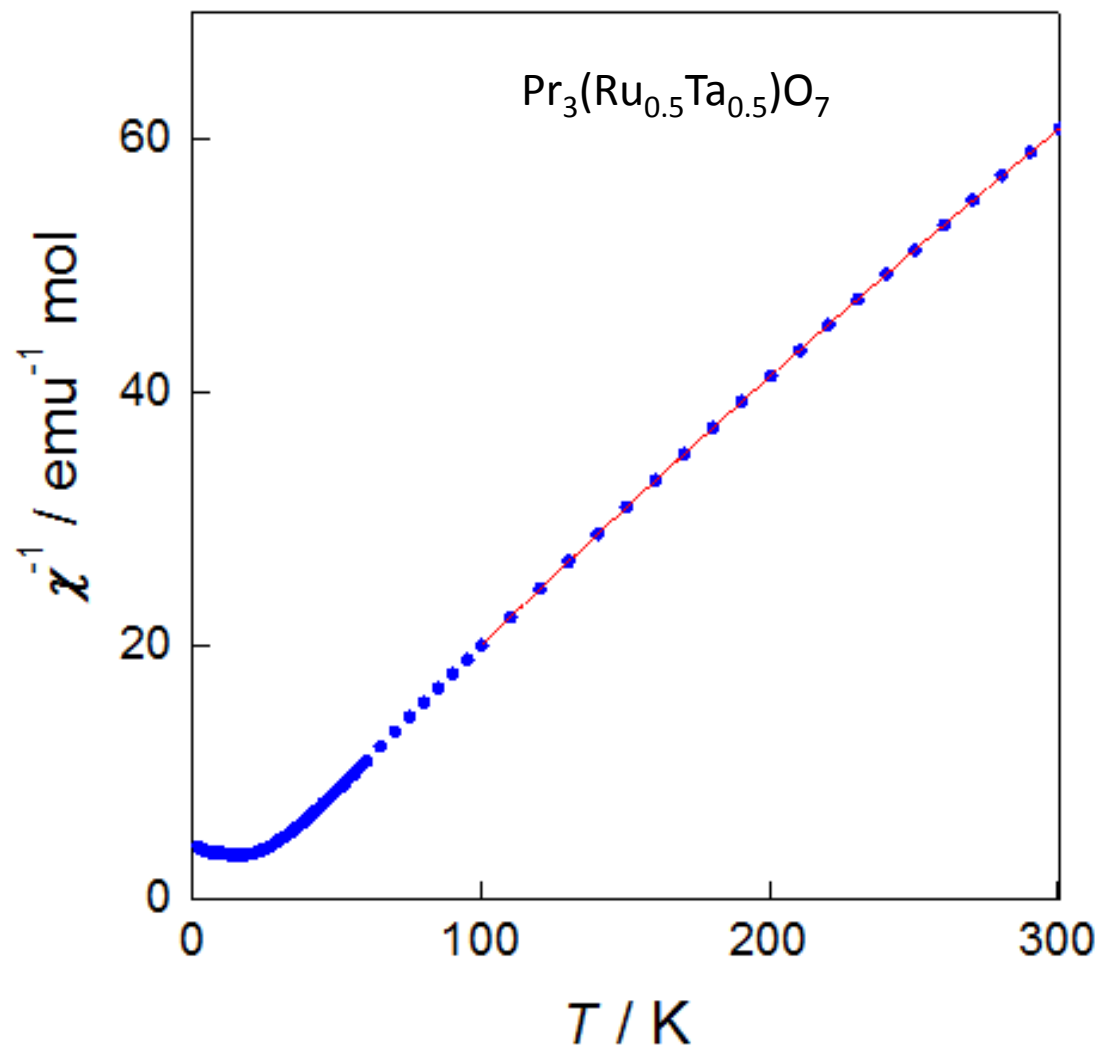


Fig.6

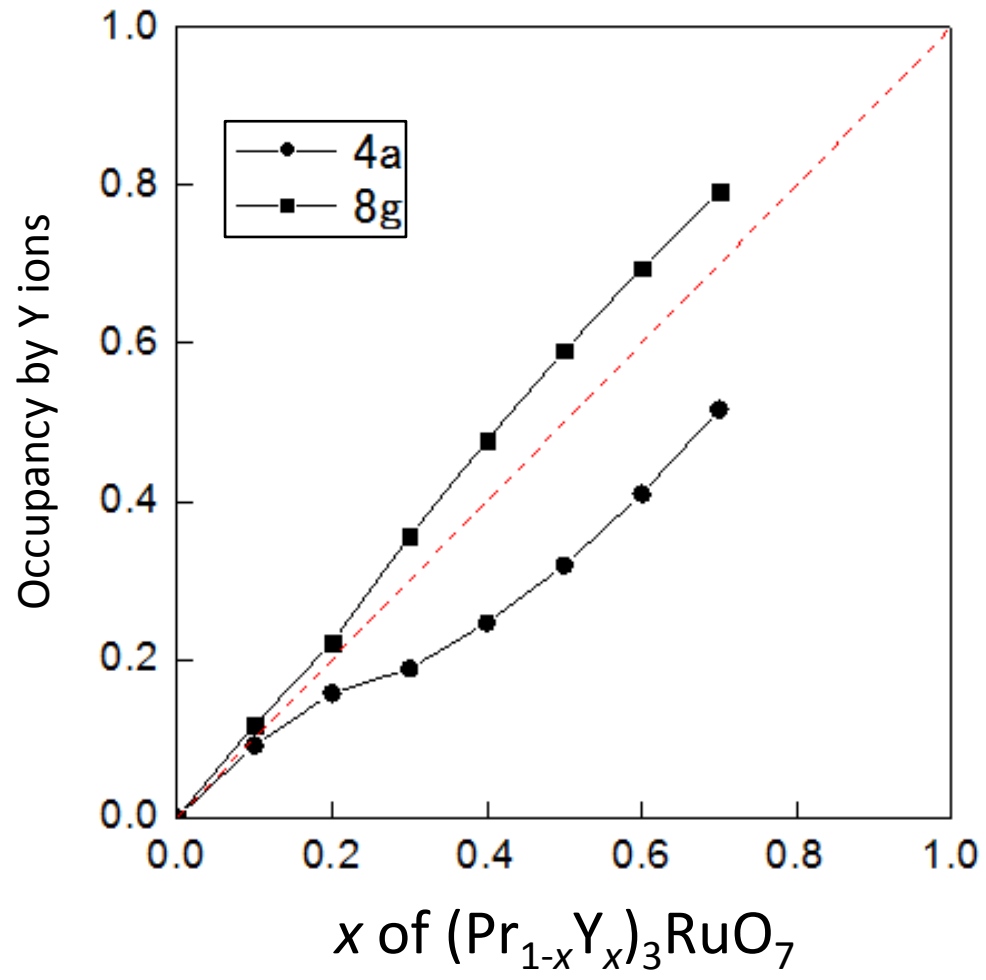


Fig. 7

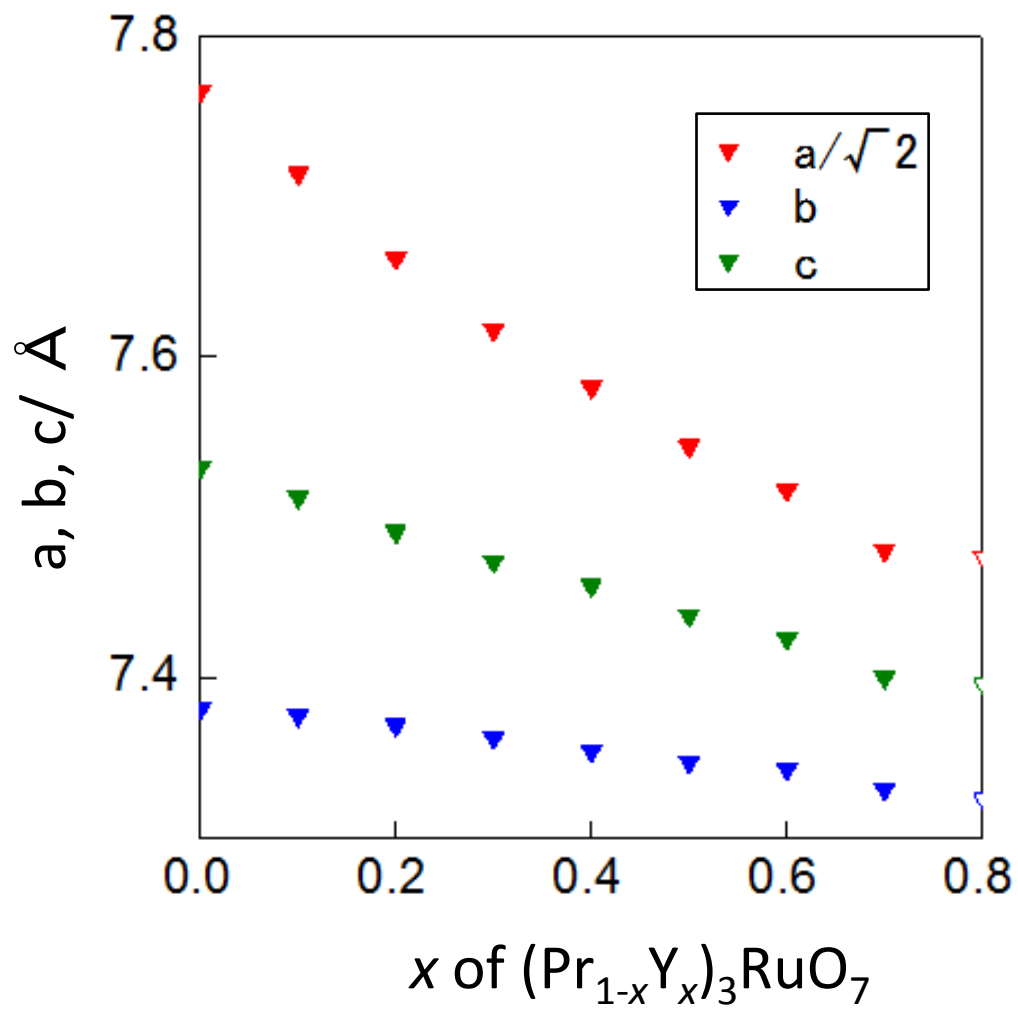


Fig.8

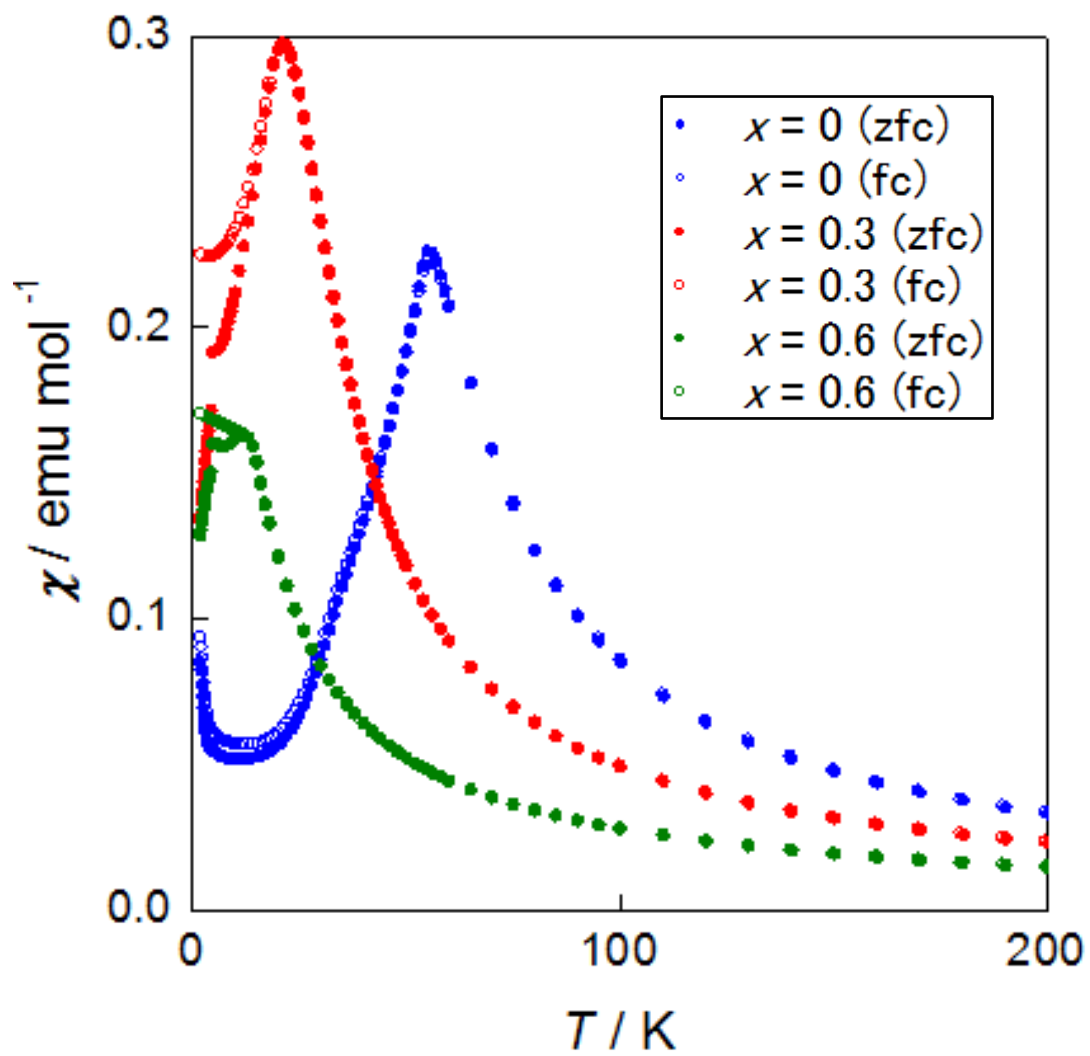


Fig.9

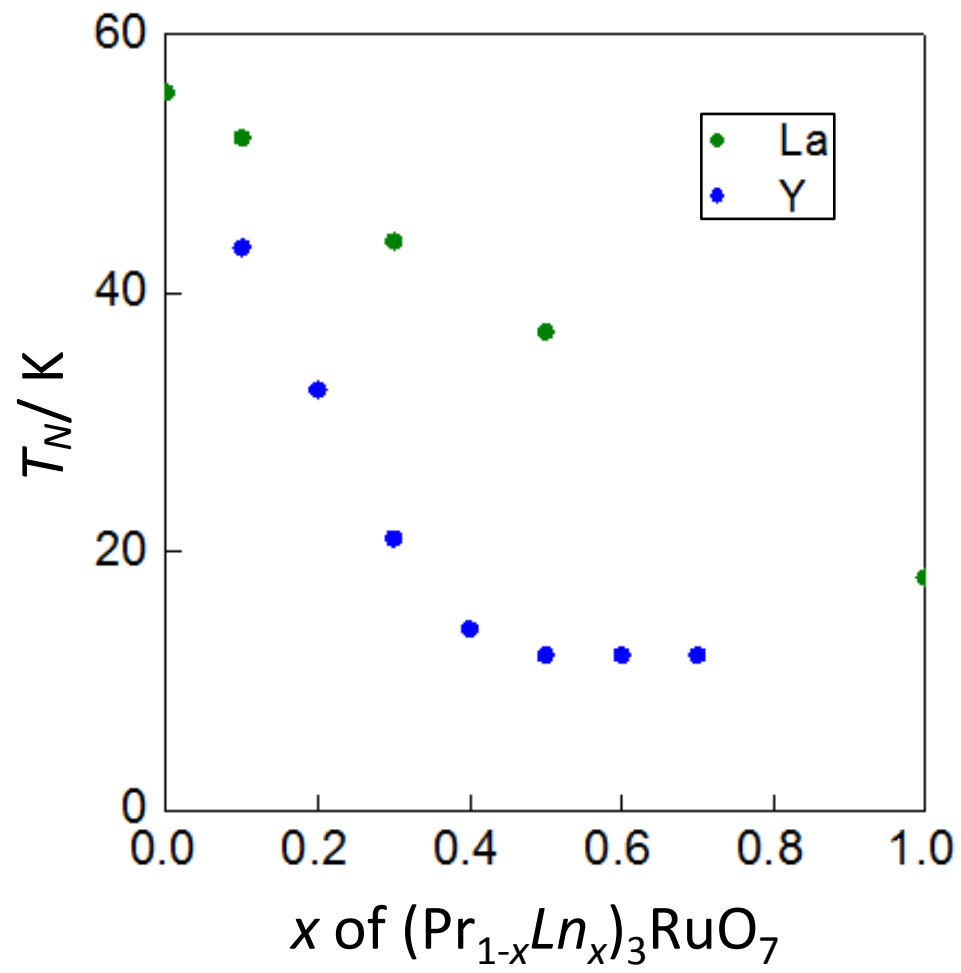


Fig.10

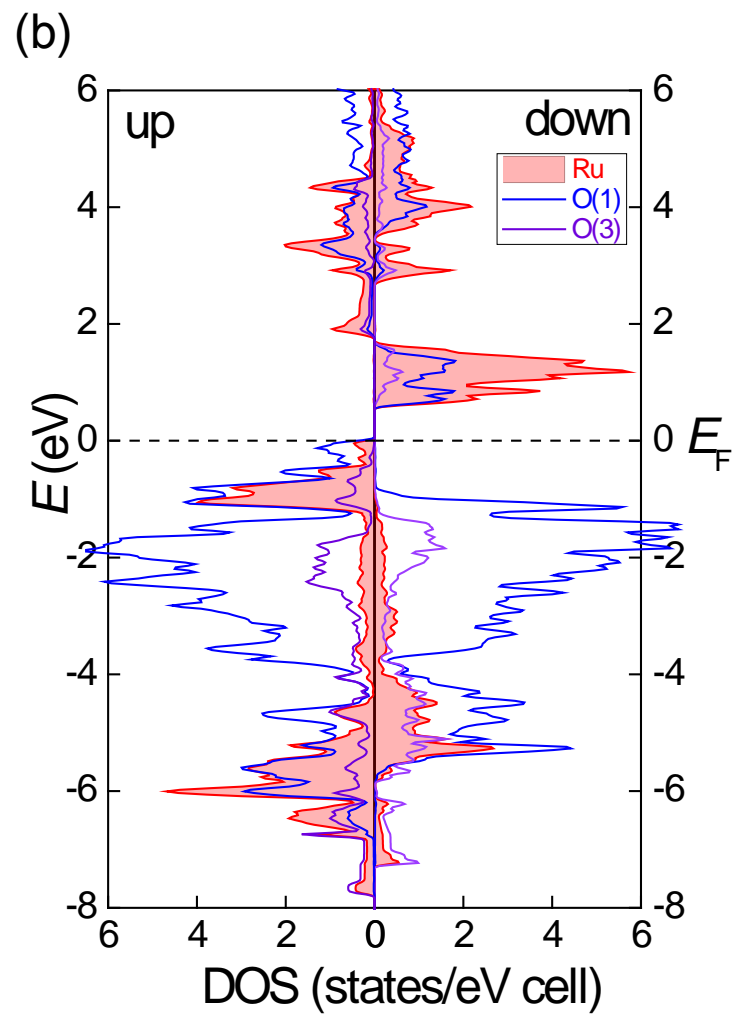
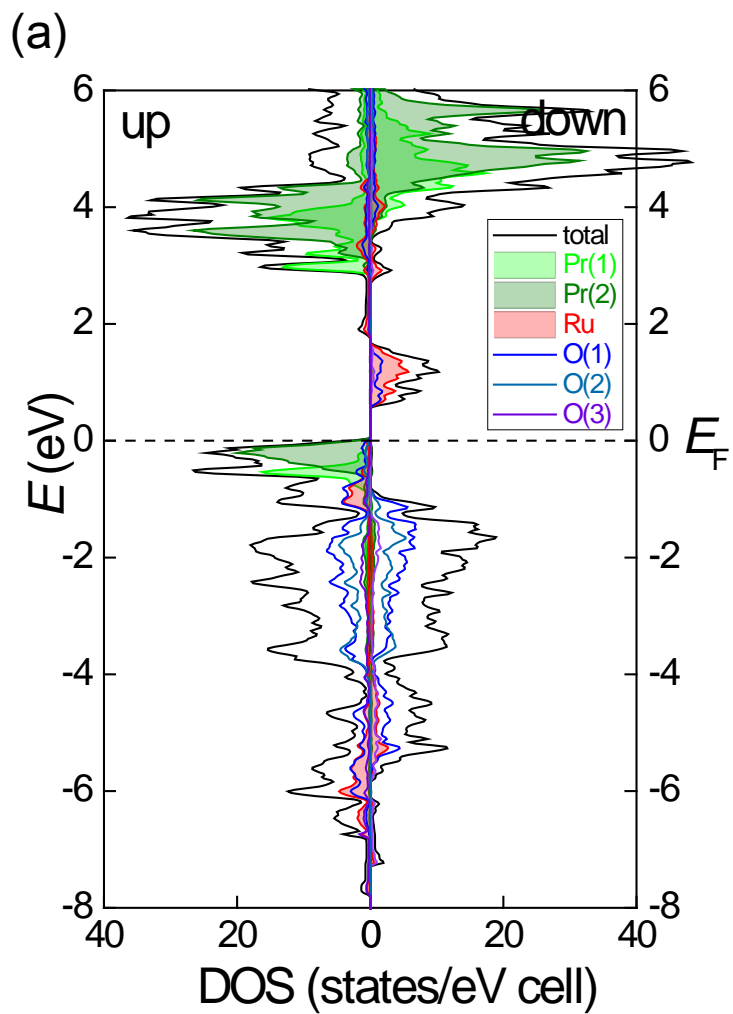


Fig.11

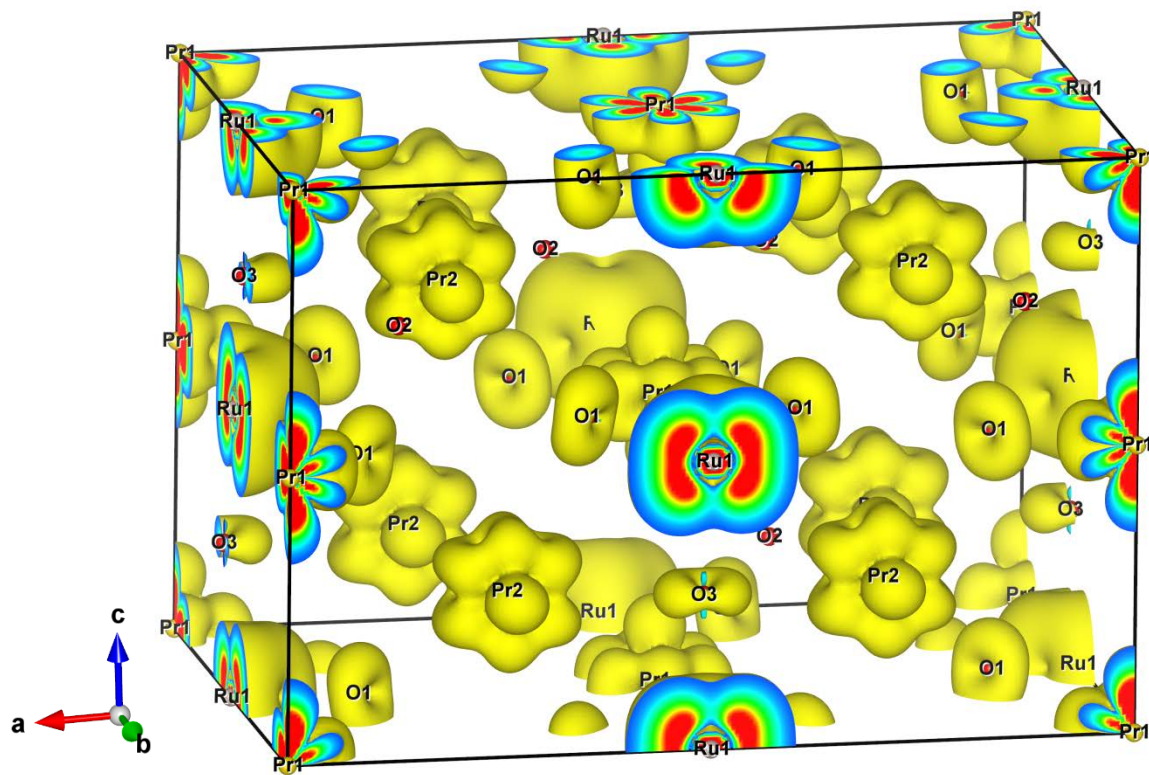


Fig.12